
Neutral iron line in the supernova remnant IC 443 and implications for MeV cosmic rays

Kumiko K. NOBUKAWA¹, Arisa HIRAYAMA¹, Aika SHIMAGUCHI¹,
Yutaka FUJITA², Masayoshi NOBUKAWA³, and Shigeo YAMAUCHI¹

¹Department of Physics, Faculty of Science, Nara Women's University, Kitauoyanishi-machi,
Nara, Nara 630-8506, Japan

²Department of Earth and Space Science, Graduate School of Science, Osaka University,
Toyonaka, Osaka 560-0043, Japan

³Faculty of Education, Nara University of Education, Takabatake-cho, Nara, Nara 630-8528,
Japan

*E-mail: kumiko@cc.nara-wu.ac.jp

Received (reception date); Accepted (acceptation date)

Abstract

We report a discovery of bright blob-like enhancements of an Fe I $K\alpha$ line in the northwest and the middle of the supernova remnant (SNR) IC 443. The distribution of the line emission is associated with molecular clouds interacting with the shock front, and is totally different from that of the plasma. The Fe I $K\alpha$ line has a large equivalent width. The most plausible scenario for the origin of the line emission is that the MeV protons accelerated in the shell leak into the molecular clouds and ionize the Fe atoms therein. The observed Fe I $K\alpha$ line intensity is consistent with the prediction of a theoretical model, in which MeV protons are accelerated along with GeV and TeV protons at the SNR.

Key words: X-rays: ISM — ISM: individual objects (IC 443) — cosmic rays

1 Introduction

Supernova remnants (SNRs) are believed to be an acceleration site of Galactic cosmic rays. GeV and very-high energy (VHE) gamma-rays have been detected from many SNRs (e.g. Abdo et al. 2009; H. E. S. S. Collaboration 2018) and have contributed to promote our understanding of high-energy cosmic rays (in the GeV–TeV band; hereafter HECRs) in SNRs. According to the established acceleration theory, suprathermal particles are injected into the acceleration mechanism and are accelerated to be low-energy cosmic rays (hereafter LECRs) and finally HECRs. In this context, LECRs have been a missing link of the particle acceleration in SNRs; there have been very limited information on LECRs so far in contrast to HECRs. LECRs are easily affected by solar modulation, and thus it is hard to observe them inside the solar system. A direct and robust observation is conducted only by the Voyager mission (Cummings et al. 2016). The ionization rate has provided the unique indirect information on LECRs (e.g. Indriolo & McCall 2012).

Recently, X-ray observations have demonstrated that an FeI $K\alpha$ line can be a powerful probe to investigate LECRs. Neutral Fe atoms in cold material are ionized by LECRs to radiate the FeI $K\alpha$ line at 6.4 keV. Here, the cross section of Fe K-shell ionization peaks at ~ 10 MeV and ~ 20 keV for protons and electrons, respectively (Tatischeff et al. 2012). The line intensity is simply in proportional to the density of LECRs and neutral Fe atoms. The FeI $K\alpha$ line that is most likely due to LECRs has been detected from more than 10 SNRs (Sato et al. 2014; Nobukawa et al. 2018; Bamba et al. 2018; Saji et al. 2018; Saji 2018). Most of them are known to be associated with molecular clouds (MCs; Jiang et al. 2010; Sano et al. 2015), which means that they have a lot of targets for LECRs accelerated in the SNRs.

IC 443 is a middle-aged SNR (the age is thought to be $\tau_{\text{age}} \sim 3,000\text{--}30,000$ yr; Petre et al. 1988; Olbert et al. 2001). MCs are interacting with the SNR (Cornett et al. 1977). The GeV and VHE gamma-rays were detected close to the SNR-MC interaction region (Albert et al. 2007; Acciari et al. 2009; Abdo et al. 2010; Tavani et al. 2010). Association between the gamma-rays and MCs and the spectral characteristic of pion decays indicate the hadronic origin (Abdo et al. 2010; Ackermann et al. 2013). Indriolo et al. (2010) measured H_3^+ column density in the vicinity of IC 443 and found the high ionization rate of $\zeta_2 \approx 2 \times 10^{-15} \text{ s}^{-1}$, which is about five times larger than typical Galactic values.

Those observational results suggest that IC 443 accelerates a large amount of LECRs. In fact, Hirayama et al. (2019) analyzed the Suzaku high-statistics data of the northeast part of the SNR, and succeeded in discovering the FeI $K\alpha$ line from the spectrum. IC 443 is known to

Table 1. Observation logs.

Obs.ID	Pointing direction		Observation start (UT)	Exposure (ks)
	$\alpha_{J2000.0}$ ($^{\circ}$)	$\delta_{J2000.0}$ ($^{\circ}$)		
501006010	94.2975	22.7757	2007-03-06 10:40:19	42.0
501006020	94.2972	22.4797	2007-03-07 12:22:51	44.0
505001010	93.9975	22.7552	2010-09-17 07:39:34	83.2
507015010	94.2974	22.7535	2012-09-27 05:29:48	101.8
507015020	94.3028	22.7465	2013-03-27 04:15:06	59.3
507015030	94.3026	22.7461	2013-03-31 11:44:34	131.2
507015040	94.3024	22.7479	2013-04-06 05:21:49	75.6

exhibit the recombining plasma (RP; Yamaguchi et al. 2009; Ohnishi et al. 2014; Matsumura et al. 2017; Hirayama et al. 2019). In order to explain both the RP and the FeI $K\alpha$ line, the authors proposed a scenario that the line is generated by LECRs. Since IC 443 is largely extended in appearance ($\sim 45'$) due to its closeness (~ 1.5 kpc; Welsh & Sallmen 2003) and has been well studied in many wavelengths from radio to gamma-rays, the SNR is a suitable target to develop understanding of LECRs. In this paper, by utilizing all the Suzaku data of IC 443, we report further evidence for the FeI $K\alpha$ line induced by LECRs and provide implications for acceleration of LECRs.

2 Observations and Data Reduction

The observation logs are summarized in table 1. Suzaku observed three regions of IC443: the northeast, northwest, and south regions. Hirayama et al. (2019) analyzed the northeast region. We utilized all the data of IC 443 obtained by the X-ray Imaging Spectrometer (XIS; Koyama et al. 2007). The XIS consists of four CCD cameras (XIS0, 1, 2, and 3). Each CCD is placed on the focal plane of the X-Ray Telescope (XRT; Serlemitsos et al. 2007). XIS0, 2, and 3 employ front-illuminated (FI) CCDs, and XIS1 has a back-illuminated (BI) CCD. The field of view (FOV) of the CCD is $17'8 \times 17'8$. The entire FOV of XIS2 and one-fourth of XIS0 have been out of function since 2006 November and 2009 June, respectively. We reprocessed the data by using `xispi` in the analysis software package, HEASoft 6.20, and the Suzaku calibration database (CALDB) released in 2016 February, with the standard event selection criteria for the XIS data processing. The ancillary response file (arf) and redistribution matrix file (rmf) were produced by `xissimarfgen` and `xisrmfgen` (Ishisaki et al. 2007), respectively. The non-X-ray background (NXB) was estimated by `xisnxbgen` (Tawa et al. 2008), and was subtracted from the X-ray images and spectra in this paper.

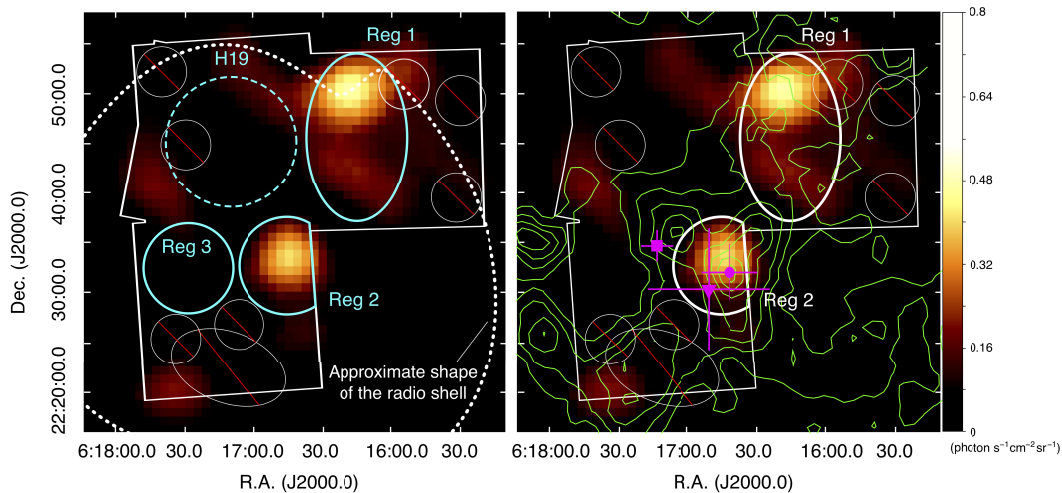


Fig. 1. Left panel: intensity profile of Fe I $K\alpha$ line. Color scale is in linear. Vignetting is corrected. The regions surrounded by white lines show the FOVs of the XIS. The dotted white line represents the approximate shape of the radio shell (Lee et al. 2008). Point sources and the PWN 1SAX J0617.1+2221, which are marked with the solid white circles and the ellipse regions, respectively, are excluded from the image (see sec.3.1). The Fe I $K\alpha$ line is enhanced in Regs 1 and 2 indicated by the solid cyan lines. We extracted X-ray spectra from the two regions, Regs 1 and 2, as well as Reg 3. Hirayama et al. (2019) detected the Fe I $K\alpha$ line in the H19 region shown by the dashed cyan circle. Right panel: Same as the left panel, but overlaid with the contours indicating the distribution of ^{12}CO ($J=1-0$) at -18 – $+10$ km s⁻¹ (Yoshiike 2019, private communication). The magenta marks and crosses represent the centroids of gamma-ray sources observed by Fermi (square), MAGIC (circle), and VERITAS (triangle) and their position errors (Albert et al. 2007; Acciari et al. 2009; Abdo et al. 2010).

3 Analysis

3.1 Fe I $K\alpha$ intensity map

The left panel of figure 1 shows the Fe I $K\alpha$ line intensity map with the binning size of 48×48 pixels (0.8×0.8 arcmin²) and Gaussian smoothing with $\sigma = 3$ bins. Vignetting is corrected. The point sources and the pulsar wind nebula (PWN) 1SAX J0617.1+2221 reported in the previous works (Bocchino & Bykov 2001, 2003) are excluded from the image. The dotted line approximates the radio shell (Lee et al. 2008). The notable structure of the intensity map is bright blob-like enhancements located in the northwest (hereafter Reg 1) and the middle of IC 443 (Reg 2). Especially, the north part of Reg 1 is the brightest enhancement, which is located near the radio shell. The region where Hirayama et al. (2019) detected the Fe I $K\alpha$ line is indicated by the dashed cyan circle (hereafter H19). In the right panel of figure 1, we overlaid the distribution of ^{12}CO ($J=1-0$) (Yoshiike 2019, private communication) with the Fe I $K\alpha$ line intensity map. Reg 1 overlaps the elongate MC whereas Reg 2 coincides with the dense core of the MC.

3.2 Spectral analysis

We extracted spectra from Regs 1 and 2, as well as Reg 3 for reference (see figure 1). Since our objective is investigation of the FeI $K\alpha$ line, we focused on the hard-band spectra (4–10 keV). Here we utilized only the FI spectra because the BI data have poor signal-to-noise ratio above 7 keV due to the large NXB. The fitting model consists of bremsstrahlung, a power-law component with the FeI $K\alpha$ and $K\beta$ lines, the FeXXV and FeXXVI $K\alpha$ lines, and the cosmic X-ray background (CXB). Due to the broad point spread function of the XRT, the contamination of the flux from the PWN 1SAX J0617.1+2221 cannot be ignored, especially for Regs 2 and 3 because of their proximity to the bright source. We simulated the contamination flux by `xissimarfgen` by using the morphology and the flux of the PWN reported in Bocchino & Bykov (2001).

It was hard to constrain the electron temperature (kT_e) in the hard-band fitting. Previous works obtained $kT_e \sim 0.6$ keV (Yamaguchi et al. 2009; Ohnishi et al. 2014; Matsumura et al. 2017; Hirayama et al. 2019), and thus we fixed kT_e to be 0.6 keV. Also we could not constrain photon index (Γ) of the power-law component, and Γ is fixed to 2.5 in the same way as Hirayama et al. (2019). The parameters of the CXB model are fixed to the values in Kushino et al. (2002). The line energies of the Gaussians were in principle free parameters for FeI, FeXXV, FeXXVI $K\alpha$ lines, but in the case that the constraint by fitting was difficult due to poor statistics, they were fixed to 6.40, 6.68, and 6.97 keV, respectively (Kaastra & Mewe 1993; Smith et al. 2001). The line center and intensity of the FeI $K\beta$ line are fixed to 7.06 keV and 0.125 times that of the FeI $K\alpha$ line (Kaastra & Mewe 1993), respectively. The line intensities of the other lines are free parameters.

The intensity of the FeI $K\alpha$ line in the individual regions are summarized in table 2. The value in H19 obtained by Hirayama et al. (2019) is also displayed for comparison. The Regs 1 and 2 spectra show a clear FeI $K\alpha$ line as are shown in figure 2, and their significance levels of the line are 3.8σ and 2.1σ , respectively. On the other hand, no significant FeI $K\alpha$ line is detected in Reg 3, and we obtained the 90% upper limit of the line intensity. For the Regs 1 and 2 spectra, we obtained the equivalent width (EW) of FeI $K\alpha$ line (the intensity ratio of the line to the power-law component): > 1.2 keV and $0.7_{-0.6}^{+0.9}$ keV, respectively, with the 90% confidence levels. As for Reg 3, the EW could not be constrained and thus is fixed to that in Reg 2. The above model explained all the spectra; the $\chi^2/\text{d.o.f.}$ of Regs 1, 2, and 3 are $8/15 = 0.53$, $16/29 = 0.55$, and $23/32 = 0.72$, respectively.

Table 2. Centroids and intensity of the Fe I $K\alpha$ line at

90% confidence levels.

Region	Centroids (keV)	Intensity (photons $\text{s}^{-1} \text{cm}^{-2} \text{sr}^{-1}$)
Reg 1	6.4 ± 0.1	0.273 ± 0.119
Reg 2	6.3 ± 0.1	0.344 ± 0.277
Reg 3	6.4 (fixed)	< 0.345
H19*	6.43 ± 0.04	0.079 ± 0.035

* The values measured by Hirayama et al. (2019).

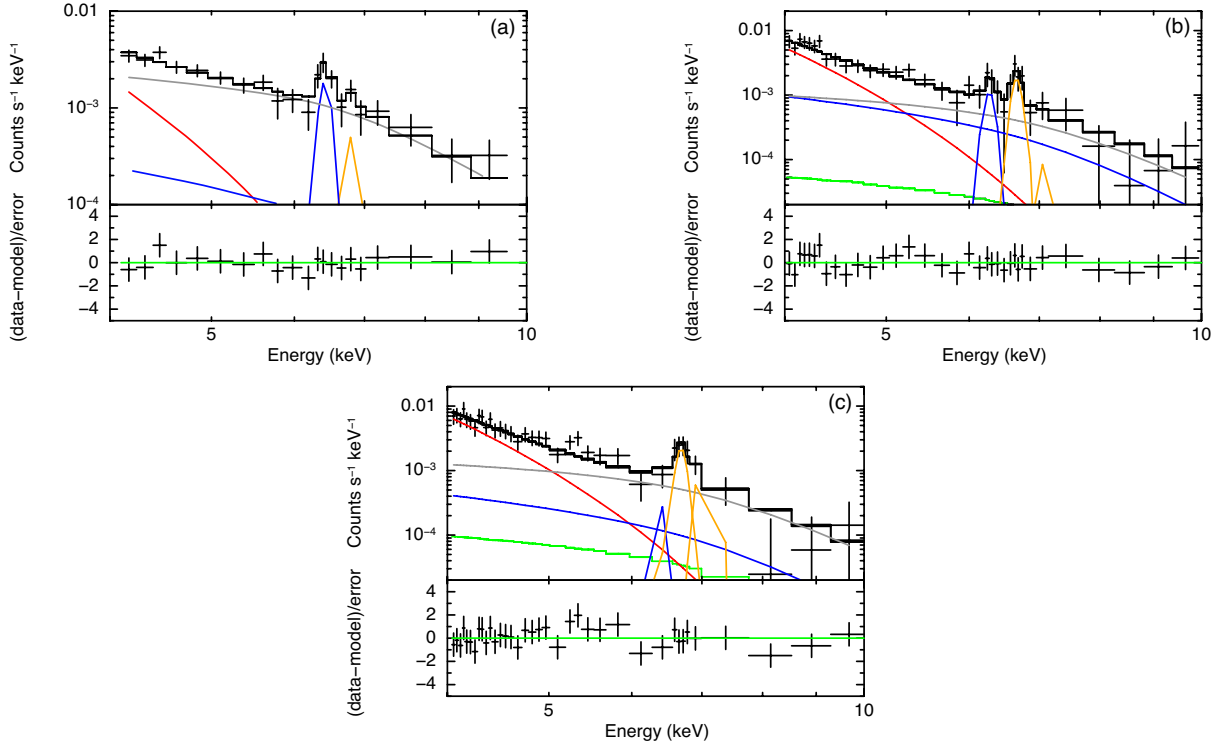


Fig. 2. X-ray spectra extracted from Reg 1 (a), Reg 2 (b) and Reg 3 (c) and the best-fit models. The solid red, blue, and orange lines are bremsstrahlung, power-law component (power law plus the Fe I $K\alpha$ line), Fe XXV and Fe XXVI $K\alpha$ lines, respectively. The gray lines indicates the CXB. The green lines in Reg 2 and Reg 3 shows the contamination flux from 1SAX J0617.1+2221.

4 Discussion

4.1 Origin of the Fe I $K\alpha$ line

We investigated the Fe I $K\alpha$ emission in IC 443 by utilizing the Suzaku data, and found the blob-like enhancement in the northeast (Reg 1) and the middle (Reg 2) of the SNR. Regs 1 and 2 are associated with interaction sites between IC 443 and MCs (the right panel of figure 1). Reg 1 is close to a bright thermal X-ray knot which seems to mark the impact of a jet-like structure of ejecta with a dense cloud (Greco et al. 2018) and Reg 2 is associated with a sharp edge in the thermal X-ray emission, just at the position of the CO cloud (e.g. Troja et al. 2006). We first discuss the origin of the Fe I $K\alpha$ line.

One possible radiation process is the collisional ionization of Fe atoms in the ionizing plasma (IP), where the Fe-rich ejecta is in a low ionization state and the Fe $K\alpha$ line at ~ 6.4 keV can be emitted (see Yamaguchi et al. 2014). In IC 443, however, the Fe $K\alpha$ band is dominated by the RP (Yamaguchi et al. 2009; Ohnishi et al. 2014; Matsumura et al. 2017; Hirayama et al. 2019). It is impossible that the RP of IC 443 radiates a detectable 6.4 keV line. In addition, the morphologies of the line intensity map (figure 1) is totally different from that of the thermal plasma (e.g. Troja et al. 2008, Matsumura et al. 2017). Those facts would also deny the plasma origin.

Since the Fe I $K\alpha$ line is associated with the MCs, another possible scenario is the inner shell ionization of neutral Fe atoms by X-rays from an external source or LECRs. The PWN 1SAX J0617.1+2221 can be a possible irradiating source. The required flux to explain the Fe I $K\alpha$ line flux is $F_X = 5 \times 10^{-11} (4\pi/\Omega)(1 \times 10^{22}/N_H)$ erg s $^{-1}$ cm $^{-2}$ in the 2–10 keV band. Here, Ω is a solid angle with which the MCs are seen from the PWN, and N_H is a hydrogen column density. The hydrogen column densities of the MCs associating with IC 443 is $(0.6\text{--}1) \times 10^{22}$ cm $^{-2}$ according to X-ray observations (Troja et al. 2006; Matsumura et al. 2017; Hirayama et al. 2019). The solid angles of Regs 1 and 2 from the PWN are ~ 0.5 sr and ~ 0.1 sr, respectively. Therefore, the required flux is estimated to be $F_X = (1\text{--}5) \times 10^{-9}$ erg s $^{-1}$ cm $^{-2}$. This is at least two orders of magnitude higher than the observed flux of 1SAX J0617.1+2221, $F_X = 6 \times 10^{-12}$ erg s $^{-1}$ cm $^{-2}$ (Bocchino & Bykov 2001).

Therefore, we propose that the Fe I $K\alpha$ line originates from LECRs that are produced by the SNR shock. Whether the LECRs are protons (with kinetic energy of the MeV band) or electrons (in the keV band) is distinguished by the EW of the Fe I $K\alpha$ line. In electron bombardment, the EW ranges in the 0.2–0.4 keV while in the proton case the EW would be > 0.6 keV (Dogiel et al. 2011). We obtained the EW of > 1.2 keV and $0.7_{-0.6}^{+0.9}$ keV for Regs 1

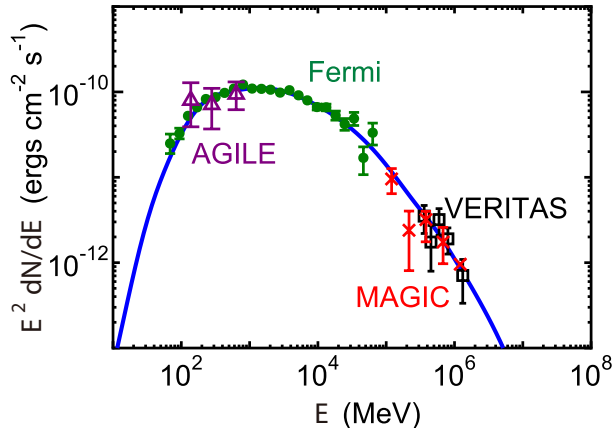


Fig. 3. Comparison of the best-fit model (solid line) with Fermi (green filled circles; Ackermann et al. 2013), VERITAS (black open squares; Acciari et al. 2009), MAGIC (red crosses; Albert et al. 2007), and AGILE (purple open triangles; Tavani et al. 2010) observations for the SNR IC 443.

and 2, respectively (section 3.2). The scenario that can explain both the regions is MeV-proton bombardment.

4.2 Comparison with Gamma-ray observations

Since SNRs are expected to accelerate CRs with various energies, MeV CR protons that we detected through the FeI $K\alpha$ line should be associated with higher-energy CRs that emit gamma-rays through proton-proton interaction. For middle-aged SNRs, GeV and VHE gamma-rays are often associated with MCs. Since Reg 2 is close to the centroid of the gamma-ray clump (the right panel of figure 1), the MeV protons that generate the FeI $K\alpha$ line may be connected to the HE CRs.

Recently, Makino et al. (2019) showed that both FeI $K\alpha$ line and gamma-ray emissions from W28 and W44 can be explained by a CR escaping model for SNRs. This model assumes that the SNRs are interacting with MCs. LECRs are currently leaking from the SNRs into the MCs and create FeI $K\alpha$ line emissions, while HE CRs had diffused out of the SNRs and generate gamma-rays through proton-proton interaction. We applied this model to IC 443; details of the model are described in Appendix. In summary, the spectrum of CRs accelerated at IC 443 is constrained by the gamma-ray spectrum (figure 3). Using the results, we calculate the FeI $K\alpha$ line intensity and find that it should be $0.29^{+0.10}_{-0.11}$ photons $s^{-1} cm^{-2} sr^{-2}$. The predicted intensity is consistent with those for Regs 1 and 2 in table 2. This supports the scenario that the observed FeI $K\alpha$ line is associated with the LECR protons that are accelerated along with the HE CRs.

5 Conclusion

We discovered the bright blob-like enhancements of the Fe I $K\alpha$ line located in the northwest and the middle of IC 443. The most plausible origin of the Fe I $K\alpha$ line is that the LECR protons accelerated in the SNR leak into the MCs and ionize the Fe atoms therein. The observed line intensity is consistent with the value expected by the gamma-ray spectra and a CR escaping model.

Acknowledgments

We thank all the members of the Suzaku teams. We also thank Professor Katsuji Koyama for valuable comments. We are grateful to Dr. Hidetoshi Sano for providing the CO data shown in figure 1. K.K.N. is supported by Research Fellowships of JSPS for Young Scientists. This work was supported by JSPS and MEXT KAKENHI Grant Numbers JP16J00548 (KKN), 18K03647 (YF) and JP17K14289 (MN).

Appendix. Application of the CR escaping model to Gamma-rays and Fe I $K\alpha$ line in IC 443

We assume that MCs with density n_{H} are distributed around the SNR in a shell region between $r = L_1$ and $r = L_2$ with a filling factor f_{gas} (see figure 1b of Makino et al. 2019). From CO observations with NANTEN2, we assume that $n_{\text{H}} = 730 \text{ cm}^{-3}$, $L_1 = 12 \text{ pc}$, $L_2 = 15 \text{ pc}$, and $f_{\text{gas}} = 0.05$ (Yoshiike 2019, private communications). For these parameters, the mass of MCs is $6.2 \times 10^3 M_{\odot}$. The distance to IC 443 is assumed to be 1.5 kpc (Welsh & Sallmen 2003). The SNR contacts with the MCs at the radius L_1 . The SNR is assumed to be in the Sedov phase and the evolution is the same as those for W28 and W44 (Makino et al. 2019). Thus, the current time is $t_{\text{obs}} = 1.5 \times 10^4 \text{ yr}$ after the supernova explosion. The momentum of escaping CRs, p_{esc} , is a decreasing function of the shock radius R_{sh} :

$$p_{\text{esc}}(t) = p_{\text{max}} \left(\frac{R_{\text{sh}}(t)}{R_{\text{Sedov}}} \right)^{-\alpha}, \quad (\text{A1})$$

where p_{max} and R_{Sedov} are the escape momentum and the shock radius at the beginning of the Sedov phase ($t = t_{\text{Sedov}}$), respectively, and α is the index that is empirically derived. We assume that $R_{\text{Sedov}} = 2.1 \text{ pc}$, $t_{\text{Sedov}} = 210 \text{ yr}$ and $\alpha = 6.5$ as we did in Makino et al. (2019). At present ($t = t_{\text{obs}}$), CRs with momenta of $p > p_{\text{esc}}(t_{\text{obs}})$ have gradually escaped from the SNR, while those with $p < p_{\text{esc}}(t_{\text{obs}})$ have been confined around the shock front. However, since the shock collides with MCs at $t \sim t_{\text{obs}}$ and the MCs prevent the CR confinement, the lower-momentum CRs are now escaping altogether. As a result, the CR momentum spectrum have a break at $p = p_{\text{esc}}(t_{\text{obs}})$, which results in a bend in the gamma-ray spectrum at $E \sim \text{GeV}$ (see figure 3).

For the above parameters for the MCs and the SNR, we calculate gamma-ray spectra

and compare them with the observed ones. Then, we constrain our model parameters for CRs through χ^2 fitting. In Makino et al. (2019), the fitting parameters are the total CR energy $E_{\text{CR,tot}}$, the index s of the CR momentum spectrum at the shock front ($\propto p^{-s}$), and the maximum momentum p_{max} [equation (A1)]. In this study, we also treat parameters associated with CR diffusion as fitting parameters because of the following reasons.

The diffusion of CRs outside the SNR is calculated based on the model of Ohira et al. (2011). We assume that the diffusion coefficient has a form given by

$$D(p) = 10^{28} \chi \left(\frac{pc}{10 \text{ GeV}} \right)^\delta \text{ cm}^{-2} \text{ s}^{-1}, \quad (\text{A2})$$

where χ (< 1) is a constant that accounts for a possible suppression of the diffusion coefficient around SNRs (Fujita et al. 2009, 2010, 2011). Makino et al. (2019) adopted $\chi = 0.5$ and $\delta = 1/3$ for W28 and W44. However, we found that these parameters cannot reproduce the convex shape of the gamma-ray spectrum of IC 443 at $\gtrsim 1$ GeV (figure 3). We note that the gamma-ray spectra for W28 and W44 are approximately represented by a power-law at $\gtrsim 1$ GeV (Makino et al. 2019). The spectrum shape for IC 443 may indicate that the diffusion coefficient or χ is much smaller than that for W28 and W44. If χ is much smaller than 0.5, lower-energy CRs remain close to the shock front and their distribution depends on the finite size of the SNR. On the other hand, higher-energy CRs can diffuse away relatively fast because the diffusion coefficient is an increasing function of energy for $\delta > 0$ [equation (A2)]. Thus, their distribution is not much different from the one when the SNR is approximated as a point CR source. The boundary of energy creates another break in the CR momentum spectrum, which is referred to as $p_{\text{br,ext}}$ in Ohira et al. (2011). In this study, we treat χ and δ as fitting parameters.

Through the parameter fitting, we obtain $E_{\text{CR,tot}} = 3.1_{-0.5}^{+0.5} \times 10^{50}$ erg, $s = 2.52_{-0.20}^{+0.10}$, $p_{\text{max}}c = 4.0_{-2.0}^{+3.9} \times 10^{13}$ eV, $\chi = 0.011_{-0.002}^{+0.003}$ and $\delta = 0.58_{-0.08}^{+0.07}$, and the best-fit result is shown in figure 3. From the results, we also obtain $p_{\text{esc}}(t_{\text{obs}}) = 6.2_{-3.1}^{+6.2} \times 10^8$ eV, which corresponds to the peak of the gamma-ray spectrum in figure 3. The small diffusion coefficient we adopted results in another break in the gamma-ray spectrum at $E \sim 10$ GeV because $p_{\text{br,ext}}c \sim 50$ GeV (figure 3). Moreover, we find that the intensity of the Fe I $K\alpha$ line is $I_{6.4\text{keV}} = 0.29_{-0.11}^{+0.10}$ photons $\text{s}^{-1} \text{ cm}^{-2} \text{ sr}^{-1}$. The line intensity is consistent with our observational results (Regs 1 and 2 in table 2).

The gamma-ray maxima appear to coincide with Reg 2 (figure 1). The distribution function of escaped HECRs is generally represented by a gaussian, $\propto \exp(-r^2/r_{\text{diff}}^2)$, where r is the distance from the SNR center and r_{diff} is the diffusion radius (e.g. equation (9) of Atayan et al. 1995). Since $R_{\text{sh}} < r_{\text{diff}}$, the HECR density is almost constant for $R_{\text{sh}} < r < r_{\text{diff}}$. In our model, the gamma-rays are emitted from the MCs in that region and Fe I $K\alpha$ line is observed in

MCs that are in touch with the SNR ($r \sim R_{\text{sh}}$). Thus, it is likely that gamma-rays and the Fe I $K\alpha$ line are observed in the same MCs. Moreover, projection effects may also be responsible for the spatial co-location of the gamma-rays and the Fe I $K\alpha$ line.

Assuming a point CR source, we can discuss the diffusion coefficient based on the size of the Fe I $K\alpha$ line emission region for Reg 2. The diffusion time t_{diff} of protons is given by $t_{\text{diff}} \sim R^2/6D'$, where D' is the diffusion coefficient and R is the size of the Fe I $K\alpha$ line emission. Figure 1 indicates that the angular sizes of Reg 2 is $4'$, which corresponds to $R = 2$ pc (assuming that the distance of IC 443 is 1.5 kpc; Welsh & Sallmen 2003). According to the equations (4.24) of Mannheim & Schlickeiser (1994) and the equation (C3) of Strong & Moskalenko (1998), the ionization cooling time of 10 MeV protons is estimated to be $t_{\text{cool}} \sim 500$ yr for Reg 2 with $n_H = 730 \text{ cm}^{-3}$ (Yoshiike 2019, private communication). The diffusion coefficient is required to be $D' \geq 4 \times 10^{26} \text{ cm}^{-2} \text{ s}^{-1}$ from the condition of $t_{\text{diff}} \leq t_{\text{cool}}$. This is much larger than the coefficient at the kinetic energy of 10 MeV ($D(p \approx 137 \text{ MeV}/c) = 9 \times 10^{24} \text{ cm}^{-2} \text{ s}^{-1}$) given by equation (A2) with $\chi = 0.011$ and $\delta = 0.58$.

We note that even if the reality is $D' \gg D(p)$, it would be allowed. In that case, the apparent inconsistency may show the difference of the diffusion coefficient between the inside and the outside of the MC. Moreover, the CRs may not be injected into the MC from a point source. For example, the size of the Fe I $K\alpha$ line emission may reflect the area of interaction between the shock and the MC, from which the CRs are injected.

References

- Abdo, A. A., et al. 2009, ApJS, 183, 46
 Abdo, A. A., et al. 2010, ApJ, 712, 459
 Acciari, V. A., et al. 2009, ApJ, 698, L133
 Ackermann, M., et al. 2013, Science, 339, 807
 Albert, J., et al. 2007, ApJ, 664, L87
 Atoyan, A. M., Aharonian, F. A., & Völk, H. J. 1995, Phys. Rev. D, 52, 3265
 Bamba, A. et al. 2018, ApJ, 854, 71
 Bocchino, F., & Bykov, A. M. 2001, A&A, 376, 248
 Bocchino, F., & Bykov, A. M. 2003, A&A, 400, 203
 Cornett, R. H., Chin, G., & Knapp, G. R. 1977, A&A, 54, 889
 Cummings, A. C., et al. 2016, ApJ, 831, 18
 Dogiel, V., Chernyshov, D., Koyama, K., Nobukawa, M., & Cheng, K -S. 2011 PASJ, 63, 535

Fujita, Y., Ohira, Y., Tanaka, S. J., & Takahara, F. 2009, *ApJL*, 707, L179

Fujita, Y., Ohira, Y., & Takahara, F. 2010, *ApJL*, 712, L153

Fujita, Y., Takahara, F., Ohira, Y., & Iwasaki, K. 2011, *MNRAS*, 415, 3434

Greco, E., Miceli, M., Orlando, S., Peres, G., Troja, E., & Bocchino, F. 2018, *A&A*, 615, A157

H. E. S. S. collaboration, 2018, *A&A*, 612, A1

Hirayama, A., Yamauchi, S., Nobukawa, K. K., Nobukawa, & M., Koyama, K., *PASJ*, 71, 37

Indriolo, N. et al. 2010, *ApJ*, 724, 1357

Indriolo, N., & McCall, B. J. 2012, *ApJ*, 745, 91

Ishisaki, Y., et al. 2007, *PASJ*, 59, S113

Jiang, B., Chen, Y., Wang, J., Su, Y., Zhou, X., Safi-Harb, S., & DeLaney, T. 2010, *ApJ*, 712, 1147

Kaastra, J. S., & Mewe, R. 1993, *A&A*, 97, 443

Koyama, K., et al. 2007, *PASJ*, 59, S23

Kushino, A., et al. 2002, *PASJ*, 54, 327

Lee, J. J., Koo, B. C., Yun, M. S., Stanimirović, S., Heiles, C., & Heyer, M. 2008, *AJ*, 135, 796

Makino, K., Fujita, Y., Nobukawa, K. K., Matsumoto, & H., Ohira, Y. 2019, *PASJ* accepted

Mannheim, K., & Schlickeiser, R. 1994, *A&A*, 286, 983

Matsumura, H., Tanaka, T., Uchida, H., Okon, H., & Tsuru, T. G. 2017, *ApJ*, 851, 73

Nobukawa, K. K., et al. 2018, *ApJ*, 854, 87

Ohira, Y., Murase, K., & Yamazaki, R. 2011, *MNRAS*, 410, 1577.

Ohnishi, T., et al. 2014, *ApJ*, 784, 74

Olbert, C. M., Clearfield, C. R., Williams, N. E., Keohane, J. W., & Frail, D. A. 2001, *ApJ*, 554, L205

Petre, R., Szymkowiak, A. E., Seward, F. D., & Willingale R. 1988, *ApJ*, 335, 215 56, 3614

Saji, S., Matsumoto, H., Nobukawa, M., Nobukawa, K. K., Uchiyama, H., Yamauchi, S., & Koyama, K. 2018, *PASJ*, 70, 23

Saji, S., Doctoral dissertation, Nagoya University, 2018

Sano, H., et al. 2015, *Revolution in Astronomy with ALMA: The Third Year*, ed. Daisuke Iono, Kenichi Tatematsu, Al Wootten, & Leonardo Testi, *ASP Conference Series*, 499

Sato, T., Koyama, K., Takahashi, T., Odaka, H., & Nakashima, S. 2014, *PASJ*, 66, 124

Serlemitsos, P. J., et al. 2007, *PASJ*, 59, S9

Smith, R. K., Brickhouse, N. S., Liedahl, D. A., & Raymond, J. C. 2001, *ApJL*, 556, L91

Strong, A. W., & Moskalenko, I. V. 1998, *ApJ*, 509, 212

Tatischeff, V., Decourchelle, A., & Maurin, G. 2012, *A&A*, 546, A88

Tavani, M., et al. 2010, *ApJ*, 710, L151.

Tawa, N., et al. 2008, *PASJ*, 60, S11

Troja, E., Bocchino, & Reale, F. 2006, ApJ, 649, 258

Troja, E., Bocchino, F., Miceli, M., & Reale, F. 2008, A&A, 485, 777

Yamaguchi, H., Ozawa, M., Koyama, K., Masai, K., Hiraga, J. S., Ozaki, M., & Yonetoku, D. 2009,
ApJL, 705, L6

Yamaguchi, H., et al. 2014, ApJL, 785, L27

Welsh, B. Y., & Sallmen, S. 2003, A&A, 408, 545